AGU PUBLICATIONS

JGR

Journal of Geophysical Research: Space Physics

RESEARCH ARTICLE

10.1002/2016JA022859

Multimodel comparison of the ionosphere variability during the 2009 sudden stratosphere warming

N. M. Pedatella[1], T.-W. Fang[2], H. Jin[3], F. Sassi[4], H. Schmidt[5], J. L. Chau[6], T. A. Siddiqui[7,8], and L. Goncharenko[9]

[1]COSMIC Program Office, University Corporation for Atmospheric Research, Boulder, Colorado, USA, [2]CIRES, University of Colorado Boulder, Boulder, Colorado, USA, [3]National Institute of Information and Communications Technology, Tokyo, Japan, [4]Space Science Division, Naval Research Laboratory, Washington, District of Colombia, USA, [5]Max Planck Institute for Meteorology, Hamburg, Germany, [6]Leibniz Institute of Atmospheric Physics, Rostock University, Kühlungsborn, Germany, [7]GFZ German Research Centre for Geosciences, Potsdam, Germany, [8]Institute of Earth and Environmental Science, University of Potsdam, Potsdam, Germany, [9]Haystack Observatory, Massachusetts Institute of Technology, Westford, Massachusetts, USA

Key Points:
- Compare different ionosphere model simulations with observations for the 2009 SSW
- Simulations capture broad features of SSW, but model-model and model-data discrepancies are apparent
- Differences can partly be attributed to differences in the simulated middle atmospheres

Correspondence to:
N. M. Pedatella,
nickp@ucar.edu

Citation:
Pedatella, N. M., T.-W. Fang, H. Jin, F. Sassi, H. Schmidt, J. L. Chau, T. A. Siddiqui, and L. Goncharenko (2016), Multimodel comparison of the ionosphere variability during the 2009 sudden stratosphere warming, *J. Geophys. Res. Space Physics*, *121*, 7204–7225, doi:10.1002/2016JA022859.

Received 25 APR 2016
Accepted 11 JUL 2016
Accepted article online 18 JUL 2016
Published online 28 JUL 2016

Abstract A comparison of different model simulations of the ionosphere variability during the 2009 sudden stratosphere warming (SSW) is presented. The focus is on the equatorial and low-latitude ionosphere simulated by the Ground-to-topside model of the Atmosphere and Ionosphere for Aeronomy (GAIA), Whole Atmosphere Model plus Global Ionosphere Plasmasphere (WAM+GIP), and Whole Atmosphere Community Climate Model eXtended version plus Thermosphere-Ionosphere-Mesosphere-Electrodynamics General Circulation Model (WACCMX+TIMEGCM). The simulations are compared with observations of the equatorial vertical plasma drift in the American and Indian longitude sectors, zonal mean *F* region peak density (N_mF_2) from the Constellation Observing System for Meteorology, Ionosphere, and Climate (COSMIC) satellites, and ground-based Global Positioning System (GPS) total electron content (TEC) at 75°W. The model simulations all reproduce the observed morning enhancement and afternoon decrease in the vertical plasma drift, as well as the progression of the anomalies toward later local times over the course of several days. However, notable discrepancies among the simulations are seen in terms of the magnitude of the drift perturbations, and rate of the local time shift. Comparison of the electron densities further reveals that although many of the broad features of the ionosphere variability are captured by the simulations, there are significant differences among the different model simulations, as well as between the simulations and observations. Additional simulations are performed where the neutral atmospheres from four different whole atmosphere models (GAIA, HAMMONIA (Hamburg Model of the Neutral and Ionized Atmosphere), WAM, and WACCMX) provide the lower atmospheric forcing in the TIME-GCM. These simulations demonstrate that different neutral atmospheres, in particular, differences in the solar migrating semidiurnal tide, are partly responsible for the differences in the simulated ionosphere variability in GAIA, WAM+GIP, and WACCMX+TIMEGCM.

1. Introduction

It is now well recognized that the changes in the lower and middle atmospheres during sudden stratospheric warmings (SSWs) lead to the occurrence of large anomalies in the ionosphere and thermosphere [e.g., *Chau et al.*, 2011; *Yiğit and Medvedev*, 2015]. Observations have clearly demonstrated that SSWs significantly impact equatorial vertical plasma drifts [*Chau et al.*, 2009; *Fejer et al.*, 2010; *Rodrigues et al.*, 2011; *Park et al.*, 2012; *Siddiqui et al.*, 2015], low-latitude electron densities [*Goncharenko et al.*, 2010a, 2010b; *Lin et al.*, 2012, 2013; *Jonah et al.*, 2014], and also the middle- to high-latitude ionosphere [*Korenkov et al.*, 2012; *Fagundes et al.*, 2015; *Medvedeva et al.*, 2015; *Pedatella and Maute*, 2015; *Polyakova et al.* 2014; *Shpynev et al.*, 2015]. There is also evidence that SSWs perturb the thermosphere neutral density, temperature, and winds [*Funke et al.*, 2010; *Liu et al.*, 2011; *Wu and Nozawa*, 2015; *Sassi et al.*, 2016]. SSWs therefore have a broad impact across the entirety of the upper atmosphere. The impact of SSWs on the upper atmosphere can be substantial, and perturbations reaching 50–100% of the background (i.e., climatological mean) values have been observed [e.g., *Goncharenko et al.*, 2010a]. Large perturbations in the ionosphere also occur during periods of high solar activity, demonstrating that the influence of SSWs is not restricted to solar minimum, geomagnetically quiet, conditions [*Pedatella et al.*, 2012; *Goncharenko et al.*, 2013; *Fang et al.*, 2014a].

The ionospheric variability during SSWs is considered to be primarily driven by changes in atmospheric tides. In particular, enhancements in the solar semidiurnal migrating tide (*SW*2), westward propagating semidiurnal nonmigrating tide with zonal wave number 1 (*SW*1), and lunar semidiurnal migrating tide (*M*2) are considered to be the dominant drivers of the ionosphere variability [*Fang et al.*, 2012; *Pedatella and Liu*, 2013; *McDonald et al.*, 2015]. In the case of the *SW*2 and *M*2, the tidal enhancements are the result of changes in the zonal mean atmosphere which impact the tidal propagation and/or result in a quasi-resonant state of the atmosphere at the *M*2 period [*Jin et al.*, 2012; *Forbes and Zhang*, 2012]. The *SW*1 is enhanced during SSWs due to the nonlinear interaction between the *SW*2 and enhanced planetary wave 1 activity [*Liu et al.*, 2010; *Pedatella and Liu*, 2013]. The tides influence the equatorial and low-latitude ionosphere primarily by modulating the *E* region dynamo generation of electric fields. The middle- and high-latitude ionosphere variability during SSWs is thought to be related to the direct propagation of tides into the upper thermosphere [*Pedatella and Maute*, 2015] along with possible changes in thermosphere neutral composition [*Korenkov et al.*, 2012; *Shpynev et al.*, 2015]. Changes in the high-latitude zonal mean temperature during SSWs may also alter the electric fields at midlatitudes [e.g., *Pancheva and Mukhtarov*, 2011]; however, electric field changes are thought to have a relatively minor role in the midlatitude ionosphere variability during SSWs compared to other mechanisms [*Korenkov et al.*, 2012].

Owing to the spatial and temporal sampling constraints of observations, numerical simulations of SSWs are an essential tool for developing a comprehensive understanding of the middle and upper atmosphere response to SSWs. Various aspects of the upper atmosphere variability during SSWs have therefore been investigated using both idealized and realistic simulations [*Liu and Roble*, 2002; *Fuller-Rowell et al.*, 2010; *Liu et al.*, 2011; *Wang et al.*, 2011; *Jin et al.*, 2012; *Korenkov et al.*, 2012; *Fang et al.*, 2012, 2014a; *Pedatella et al.*, 2012, 2014a; *Maute et al.*, 2014; *Klimenko et al.*, 2015a; *Pedatella and Maute*, 2015; *Klimenko et al.*, 2016]. However, in order to derive conclusions from the simulations, it is important to have confidence in the simulation results and understand any potential shortcomings. To understand the potential uncertainties in model simulations, *Pedatella et al.* [2014b] recently compared the neutral dynamics of the 2009 SSW simulated by four different whole atmosphere models. Though the general features of the zonal mean, tide, and planetary wave variability were reproduced in the different whole atmosphere models, the model comparison revealed notable differences in certain aspects of the simulations, such as the tidal amplitudes.

The present paper extends the prior comparison to model simulations of the equatorial and low-latitude ionosphere during the 2009 SSW. Given the discrepancies in the neutral atmosphere simulations, along with the large differences in ionosphere model simulations during quiet [*Fang et al.*, 2014b] and geomagnetically active periods [*Shim et al.*, 2011], a comparison of the simulated ionosphere response to SSWs is warranted in order to understand the present capabilities to model ionosphere variability during SSWs. We initially consider simulations of the ionosphere that have been previously presented in the literature, namely, the Ground-to-topside model of the Atmosphere and Ionosphere for Aeronomy (GAIA) [*Jin et al.*, 2012], Whole Atmosphere Model plus Global Ionosphere Plasmasphere (WAM+GIP) [*Wang et al.*, 2014], and Whole Atmosphere Community Climate Model eXtended version plus Thermosphere-Ionosphere-Mesosphere-Electrodynamics General Circulation Model (WACCMX+TIMEGCM) [*Pedatella et al.*, 2014a]. The model simulations are compared with observations of the equatorial vertical plasma drift velocity measured directly at Jicamarca and indirectly from magnetometer observations over India, *F* region peak density (N_mF_2) from Constellation Observing System for Meteorology, Ionosphere, and Climate (COSMIC), and total electron content (TEC) from ground-based Global Positioning System (GPS) receivers. To assess the sensitivity of the modeled ionosphere to the neutral atmosphere, we perform additional simulations in the TIMEGCM with lower atmosphere forcing provided by the neutral atmosphere simulated by GAIA, Hamburg Model of the Neutral and Ionized Atmosphere (HAMMONIA), WACCMX, and WAM.

2. Model Simulations of the 2009 SSW

The 2009 SSW was one of the strongest SSWs in recent history [e.g., *Manney et al.*, 2009] and also occurred during a period of quiescent solar and geomagnetic activity. It thus represents an ideal scenario for studying coupling between atmospheric regions during SSWs. Additionally, many studies have focused on the neutral atmosphere and ionosphere variability during the 2009 SSW. The 2009 SSW is therefore considered as an important case study for understanding how well different ionospheric models are able to reproduce the ionospheric variability during SSWs. We first compare three different model simulations that have all previously been used to investigate the 2009 SSW. A description of these models is provided in sections 2.1–2.3. We have further performed four simulations where different neutral atmosphere forcings are used to simulate

the 2009 SSW in the same upper atmosphere model (TIMEGCM). These additional simulations are described in section 2.4, and provide insight into how differences in the simulated stratosphere and mesosphere may impact the ionosphere variability.

2.1. GAIA

GAIA is a fully coupled atmosphere-ionosphere general circulation model, including self-consistent electrodynamics. The neutral atmosphere in GAIA extends from the ground to the exobase ($\sim 1 \times 10^{-10}$ hPa, ~500 km), while the upper boundary of the ionospheric component is 3000 km. The reader is referred to *Jin et al.*, 2012 [2012, and references therein], for details regarding the GAIA model and the simulation of the 2009 SSW. Briefly, to reproduce the dynamical variability in the lower atmosphere, GAIA is nudged toward the full dynamical fields (i.e., zonal mean, tides, and planetary waves) of the Japanese 25 year reanalysis (JRA-25) from the surface to 12 hPa (~28 km), and is unconstrained above 12 hPa. The nudged fields include horizontal winds, temperature, surface pressure, and water vapor.

2.2. WAM+GIP

WAM extends the upper boundary of the United States National Weather Service Global Forecast System from the lower mesosphere (~60 km) to the upper thermosphere (~600 km) [*Akmaev et al.*, 2008]. WAM is constrained in the lower atmosphere by assimilating atmospheric observations using the method of three-dimensional variational (3DVAR) data assimilation [*Wang et al.*, 2011]. Only observations below ~0.1 hPa (~65 km) are assimilated in WAM, so the simulations can be considered to be unconstrained above this altitude. To simulate the ionosphere variability during the 2009 SSW, one-way coupling is performed between WAM and the GIP model. The GIP is a stand-alone ionosphere-plasmasphere model that is coupled to an electrodynamics solver [*Fang et al.*, 2009]. In the WAM+GIP simulations, the WAM neutral winds, and NRLMSISE-00 temperature and neutral composition [*Picone et al.*, 2002] provide the necessary thermosphere input to the GIP model. The NRLMSISE-00 temperature and neutral composition are used owing to the fact that the WAM neutral temperature and compositions have not yet been fully validated. The use of the empirical temperature and composition should not significantly influence the results at low latitudes since the ionosphere variability at low latitudes during SSWs is primarily due to changes in electrodynamic processes, which are driven by the neutral winds. A more detailed description of the WAM+GIP simulations of the 2009 SSW is provided by *Wang et al.* [2014].

2.3. WACCMX+TIMEGCM

WACCMX is part of the National Center for Atmospheric Research Community Earth System Model and simulates an altitude range from the surface to the upper thermosphere (2.5×10^{-9} hPa, ~500 km). The dynamical variability during the 2009 SSW is simulated by nudging the WACCMX dynamical fields toward a merged reanalysis of the Navy Operational Global Atmospheric Prediction System-Advanced Level Physics High Altitude (NOGAPS-ALPHA) and NASA Modern Era Retrospective Analysis for Research and Applications (MERRA) up to 0.002 hPa (~92 km) [*Sassi et al.*, 2013]. WACCMX does not include a self-consistent ionosphere, and in order to simulate the ionosphere variability based on WACCMX dynamical fields, *Pedatella et al.* [2014a] used WACCMX to constrain the TIMEGCM dynamical fields up to ~95 km. In this approach the TIMEGCM zonal mean fields are nudged toward the WACCMX zonal means, and the planetary waves and tidal (including the *M*2 lunar tide) perturbations are applied at the TIMEGCM lower boundary (10 hPa, ~30 km). The reader is referred to *Pedatella et al.* [2014a] for further details regarding the WACCMX+TIMEGCM simulations.

2.4. TIMEGCM Experiments

When comparing the GAIA, WAM+GIP, and WACCMX+TIMEGCM ionospheres it is difficult to determine whether differences are due to the known differences in the simulated neutral atmospheres [*Pedatella et al.*, 2014b] or are the result of different treatment of the various ionospheric processes (i.e., production, loss, transport, etc.). It is therefore beneficial to use a single ionosphere model, but with different neutral atmospheric forcing, to understand how sensitive the simulated ionosphere variability is to differences in the neutral atmosphere. We perform such a sensitivity study by nudging the TIMEGCM model up to ~95 km with the neutral atmosphere (neutral winds and temperatures) of the GAIA, HAMMONIA, WACCMX, and WAM simulations. Note that we include the HAMMONIA simulations of the 2009 SSW since it was included in the previous comparison performed by *Pedatella et al.* [2014b]. We refer the reader to *Schmidt et al.* [2006] and *Pedatella et al.* [2014b] for details regarding the HAMMONIA model and specifics of the 2009 SSW simulation.

The TIMEGCM simulations are performed by nudging the full dynamical fields (i.e., zonal mean, planetary waves, and tides) from the TIMEGCM lower boundary up to ~95 km [e.g., *Liu et al.*, 2013]. The full fields are used

in order to preserve the notable differences in the tidal amplitudes between the different neutral atmosphere simulations. We note that this is a different approach than that used for the WACCMX+TIMEGCM simulations that are described in section 2.3, and a separate simulation was performed where the WACCMX full fields (as opposed to just the zonal mean) are used to constrain the TIMEGCM. This WACCMX+TIMEGCM simulation also does not include the *M*2 lunar tide since it is not included in the other neutral atmosphere model simulations. We will refer to this simulation as WACCMX+TIMEGCM$_{ff}$ in the remainder of the text.

2.5. Summary of Main Model Differences

The preceding sections provide details about the different model simulations. In this section, we briefly summarize the main differences among the simulations that are thought to be potentially relevant to the present study.

One of the important differences among the model simulations is the method used to constrain the lower atmosphere dynamics in order to reproduce the 2009 SSW. The different approaches used are as follows: nudging up to ~30 km altitude using the JRA-25 (GAIA), 3DVAR data assimilation of lower atmosphere observations (WAM), and nudging up to ~92 km using a merged NOGAPS-ALPHA and MERRA reanalysis (WACCMX). It should be noted that the merged NOGAPS-ALPHA and MERRA reanalysis assimilates observations at mesosphere and lower thermosphere (MLT) altitudes. As discussed in *Pedatella et al.* [2014b], constraining to a higher altitude may lead to better representation of the MLT dynamics, at least in terms of the large-scale variability. Additional differences in the neutral atmosphere simulations are related to the parameterization of gravity wave drag.

We consider the main differences in the ionospheric portion of the models to be the spatial grid and the geomagnetic field. Both GAIA and TIMEGCM use a standard latitude-longitude-altitude grid while the GIP grid is based on geomagnetic field lines. The different grids will primarily impact plasma transport, and, in general, ionosphere models based on geomagnetic field lines should better reproduce the equatorial ionosphere. A dipole geomagnetic field configuration is used in GAIA, and both GIP and TIMEGCM use magnetic Apex coordinates [*Richmond*, 1995] based on the International Geomagnetic Reference Field. The different geomagnetic field configurations may be important in terms of the model capability to capture aspects of the longitudinal variability of the ionosphere, especially in longitude sectors where the magnetic field is not well represented by the dipole approximation, and also longitudes where the magnetic declination is large. The TIMEGCM upper boundary is significantly lower than the GAIA and GIP upper boundaries, which may make the TIMEGCM more sensitive to the imposed upper boundary conditions. Last, WAM+GIP and WACCMX+TIMEGCM are one-way coupled (i.e., there is no feedback from the ionosphere to the thermosphere), and GAIA is fully coupled. We note that the above is only a brief summary of the main differences among the models, and a comprehensive summary of all the differences is beyond the scope of the present study.

3. Observations

3.1. Equatorial Vertical Plasma Drift

The different model simulations are compared with the vertical plasma drift observed in the American longitude sector and derived from geomagnetic perturbations in the Indian longitude sector. The Jicamarca Radio Observatory (11.95°S and 76.87°W geographic; 1.92°S magnetic latitude) incoherent scatter radar (ISR) provides the vertical plasma drift observations in the American sector. The vertical plasma drifts are derived from 150 km echoes using the technique of *Chau and Woodman* [2004]. The drifts derived from the 150 km echoes are consistent with ISR *F* region $\mathbf{E} \times \mathbf{B}$ vertical drifts. *Chau et al.* [2009] previously studied the 2009 SSW using the Jicamarca ISR observations, and found a clear signature of the 2009 SSW in the observations.

Magnetometer observations are used in the Indian longitude sector to obtain a proxy for the vertical plasma drift perturbations that occur in this longitude sector. Following *Anderson et al.* [2002], the signature of the vertical plasma drift is obtained by differencing the horizontal component of the geomagnetic field observed at a station along the geomagnetic equator (Tirunelveli; 8.7°N and 77.8°E geographic; 0.3° magnetic latitude) with a station located ~5–10° off of the geomagnetic equator (Alibaug; 18.7°N and 72.8°E geographic; 10.3° magnetic latitude). Note that to remove the background main field the daily nighttime average is first removed from the observations. Though *Anderson et al.* [2002] determined an empirical relationship between the horizontal magnetic field perturbations (ΔH) and the vertical plasma drift velocity, we choose to present the results as magnetic field fluctuations owing to potential uncertainty in applying the empirical relationship

to a different longitude sector than where it was originally derived. The comparison of the model simulations to the magnetometer observations should therefore be considered as a qualitative comparison.

3.2. COSMIC N_mF_2

COSMIC observations of N_mF_2 are used to provide an observational baseline for the model simulations from a global perspective. COSMIC is a six-satellite constellation that uses the technique of GPS radio occultation to observe the neutral atmosphere (troposphere and stratosphere) and ionosphere [*Anthes et al.*, 2008; *Yue et al.*, 2014]. We use observations of the N_mF_2 obtained from the Abel inversion [*Lei et al.*, 2007], which show good agreement with independent ground-based observations [e.g., *McNamara and Thompson*, 2014]. To ensure adequate sampling, the COSMIC observations are binned using a 5 day running mean in 2.5° magnetic latitude and 1 h local time (LT) bins.

3.3. GPS TEC

Ground-based observations of the GPS TEC in the South American longitude sector are calculated using the MIT Automated Processing of GPS (MAPGPS) software [*Rideout and Coster*, 2006]. The MAPGPS processing provides estimates of the TEC in 1° latitude/longitude bins with a 5 min temporal resolution. For the present study, we use the GPS TEC observations at 75°W longitude, where an extensive GPS network provides excellent latitudinal coverage. We note that the ground-based GPS TEC represents the integrated electron density from the surface to ~20,000 km altitude, and the limited altitude of the model upper boundaries may therefore result in the simulations not including the entire topside ionosphere and plasmasphere contribution of the TEC. The plasmasphere can contribute up to 30–40% of the total TEC during the daytime [*Yizengaw et al.*, 2008; *Lee et al.*, 2013; *Klimenko et al.*, 2015b], and the limited altitude of the model upper boundaries can thus lead to a significant underestimation of the TEC. One should therefore consider the comparison between the model simulations and ground-based GPS TEC observations in a qualitative, rather than quantitative, sense.

4. Results and Discussion

4.1. Comparison of GAIA, WACCMX+TIMEGCM, and WAM+GIP

Perturbations in the equatorial vertical plasma drift velocity simulated by the GAIA, WACCMX+TIMEGCM, and WAM+GIP models along with the Jicamarca ISR observations are shown in Figure 1. The perturbations are calculated by removing the mean value over the entire time period separately for each local time. Removing the mean value is done to emphasize the perturbations, though it does remove absolute biases between the models and observations. A 3 day smoothing has been applied to emphasize the SSW-induced perturbations. The vertical black line in Figure 1, and all subsequent figures, indicates the timing of the SSW based on the polar vortex weakening definition (minimum zonal mean zonal wind at 70°N and 48 km) of *Zhang and Forbes* [2014]. Hereafter, we will refer to the occurrence of the polar vortex weakening as the onset of the SSW. Note that the WAM+GIP simulation begins on day 13, so no results are shown prior to this date for the WAM+GIP simulation in Figure 1 and subsequent figures. Comparing the three different model simulations with the observations reveals clear similarities, but also notable differences. Similar to the observations, ~2–3 days after the SSW onset, the model simulations all show enhanced vertical drifts in the morning and decreased drifts in the afternoon. The vertical drift perturbations are significantly stronger in WAM+GIP compared to GAIA and WACCMX+TIMEGCM, which both have drift perturbations of similar magnitude. The model simulations also all exhibit a shift of the positive/negative drift perturbations toward later local times over the course of several days. The shift of the vertical plasma drift anomalies toward later local times is again similar to the observations, and is known to be a characteristic feature of the ionosphere variability during SSWs. The shift of the positive/negative anomalies toward later local times is, however, too slow in the GAIA and WAM+GIP simulations, and these models do not display enhanced afternoon vertical drifts until approximately days 35–40, which is ~5 days delayed compared to the observations. However, the enhanced afternoon vertical plasma drifts after day ~40 that are seen in the GAIA and WAM+GIP simulations are in good agreement with the observations. The simulated local time shift following the SSW onset is significantly faster in WACCMX+TIMEGCM compared to GAIA and WAM+GIP. As demonstrated by *Pedatella et al.* [2014a], the faster local time shift is considered to be due to the inclusion of the *M*2 lunar tide in WACCMX+TIMEGCM, and this appears to result in a phase shift that is in better agreement with the observations.

The equatorial vertical drift perturbations in the Indian longitude sector simulated by the three models and the magnetometer derived ΔH are shown in Figure 2. Note that a 3 day smoothing has again been applied. The reader is reminded that the comparison between the simulated vertical drift perturbations and the ΔH should

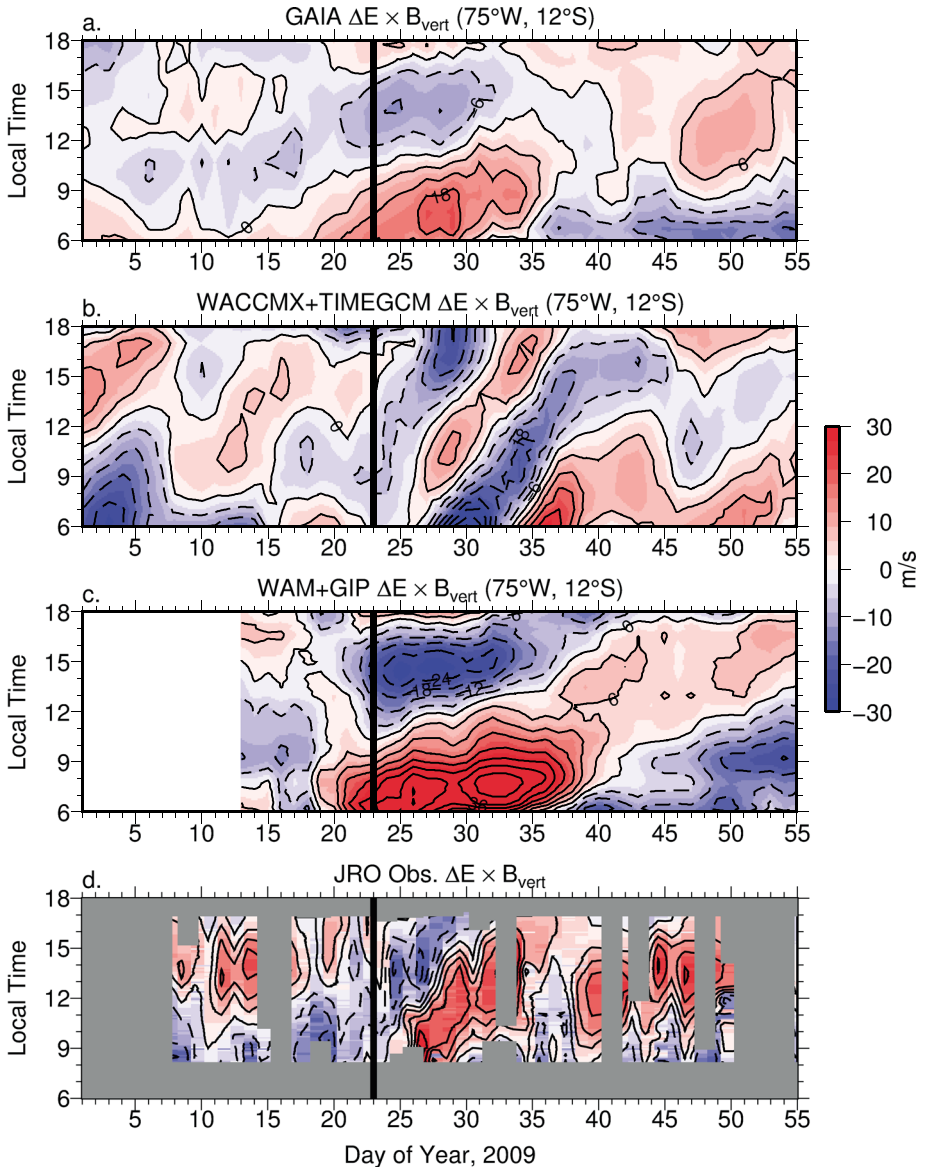

Figure 1. Perturbations in the vertical plasma drift velocity at Jicamarca, Peru (75°W, 12°S) simulated by the (a) GAIA, (b) WACCMX+TIMEGCM, and (c) WAM+GIP models. (d) The observed vertical plasma drift perturbations from the Jicamarca incoherent scatter radar. The gray areas in Figure 1d indicate periods when observations are unavailable. The solid vertical black line indicates the timing of the polar vortex weakening. Contours are every 6 m s^{-1}.

be considered only in qualitative terms. The results in Figure 2 reveal similar features as those seen in Figure 1. The observations again indicate a morning enhancement and afternoon decrease following the SSW onset. Similar to the American longitude sector, this feature progresses toward later local times in the ~5–10 days following the SSW. The GAIA and WAM+GIP models simulate a strong morning increase and afternoon decrease in the equatorial vertical plasma drifts, but do not indicate a shift of this feature toward later local times until around day 40, which is later than seen in the observations. The WACCMX+TIMEGCM simulation again appears to be the only simulation that well reproduces the shift of the vertical plasma drift perturbations toward later local times, providing further evidence that inclusion of the lunar tide may be critical for capturing this feature of the ionosphere variability during SSWs. We note that the shift of the plasma drift perturbations toward later local times could be related to a phase shift in the *SW*2. However, as shown in *Pedatella et al.* [2014b], GAIA, WAM, and WACCMX have similar phase shifts in the *SW*2 during the 2009 SSW time period. Furthermore, when the *M*2 is not included in the WACCMX+TIMEGCM simulation, the movement of the vertical plasma drift

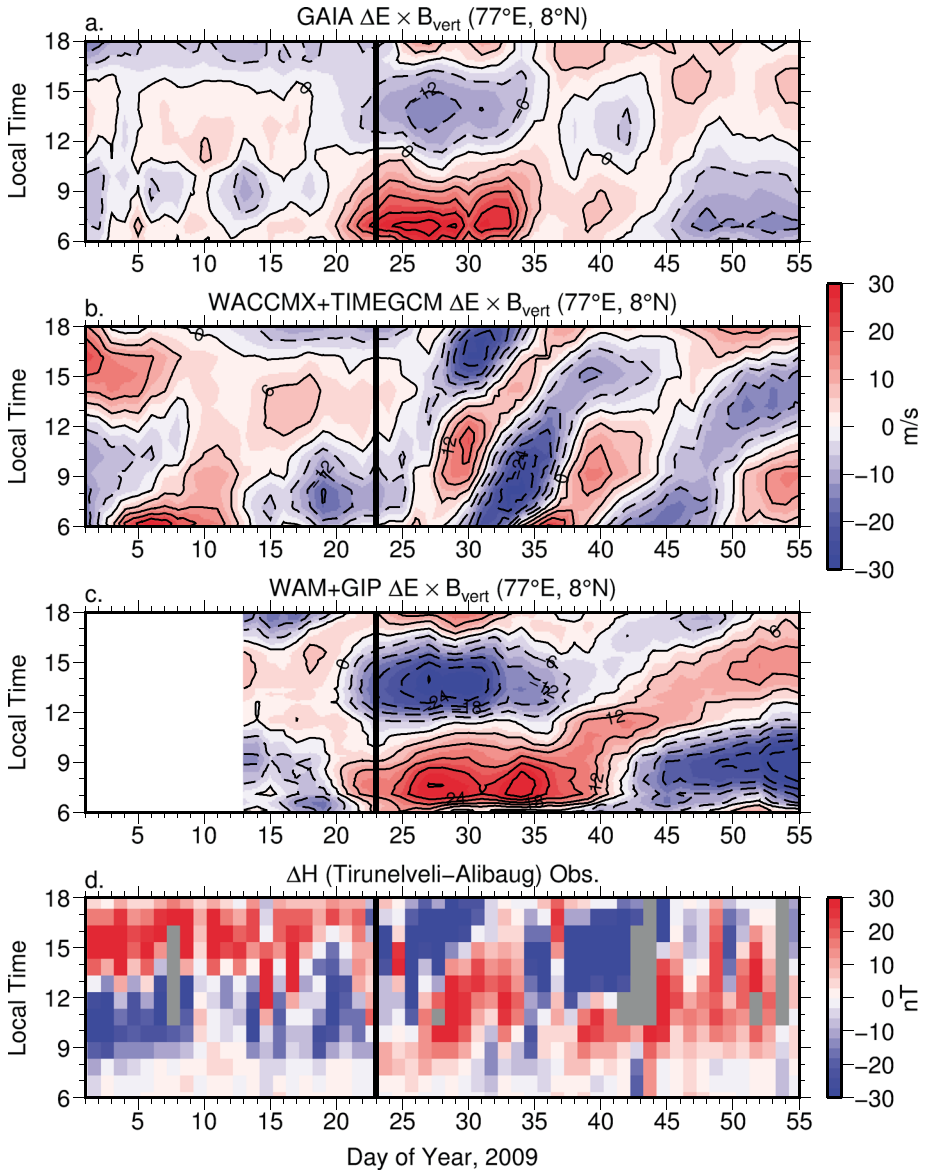

Figure 2. Perturbations in the vertical plasma drift velocity at Tirunelveli, India (77°E, 8°N) simulated by the (a) GAIA, (b) WACCMX+TIMEGCM, and (c) WAM+GIP models. (d) Observed equatorial electrojet perturbations (ΔH) from differencing magnetometer observations at Tirunelveli and Alibaug. The gray areas in Figure 2d indicate periods when observations are unavailable. The solid vertical black line indicates the timing of the polar vortex weakening. Contours are every 6 m s^{-1}.

perturbations toward later local times is no longer in good agreement with the observations (see Figures 7 and 8, which will be discussed later). We can therefore conclude that the inclusion of the lunar tide is crucial for capturing the local time variability of the vertical plasma drift perturbations. It is, however, important to recognize that the differences among the simulations are not solely due to inclusion of the lunar tide but are also related to differences in the neutral atmospheres and treatment of ionospheric processes.

Figures 3 and 4 present the zonal mean N_mF_2 from the GAIA, WACCMX+TIMEGCM, and WAM+GIP simulations along with the COSMIC observations at 1000 and 1800 local time (LT), respectively. A 5 day running mean has been applied to the simulations to be consistent with the observations. The results in Figures 3 and 4 are presented on different color scales to highlight the variability in the models, which is the focus of the present paper. There are, however, notable biases among the model simulations and observations that are also important to take into consideration. For example, a notable shortcoming of the WACCMX+TIMEGCM simulation is that the N_mF_2 is significantly smaller than the observations, and the latitudinal width of the equatorial

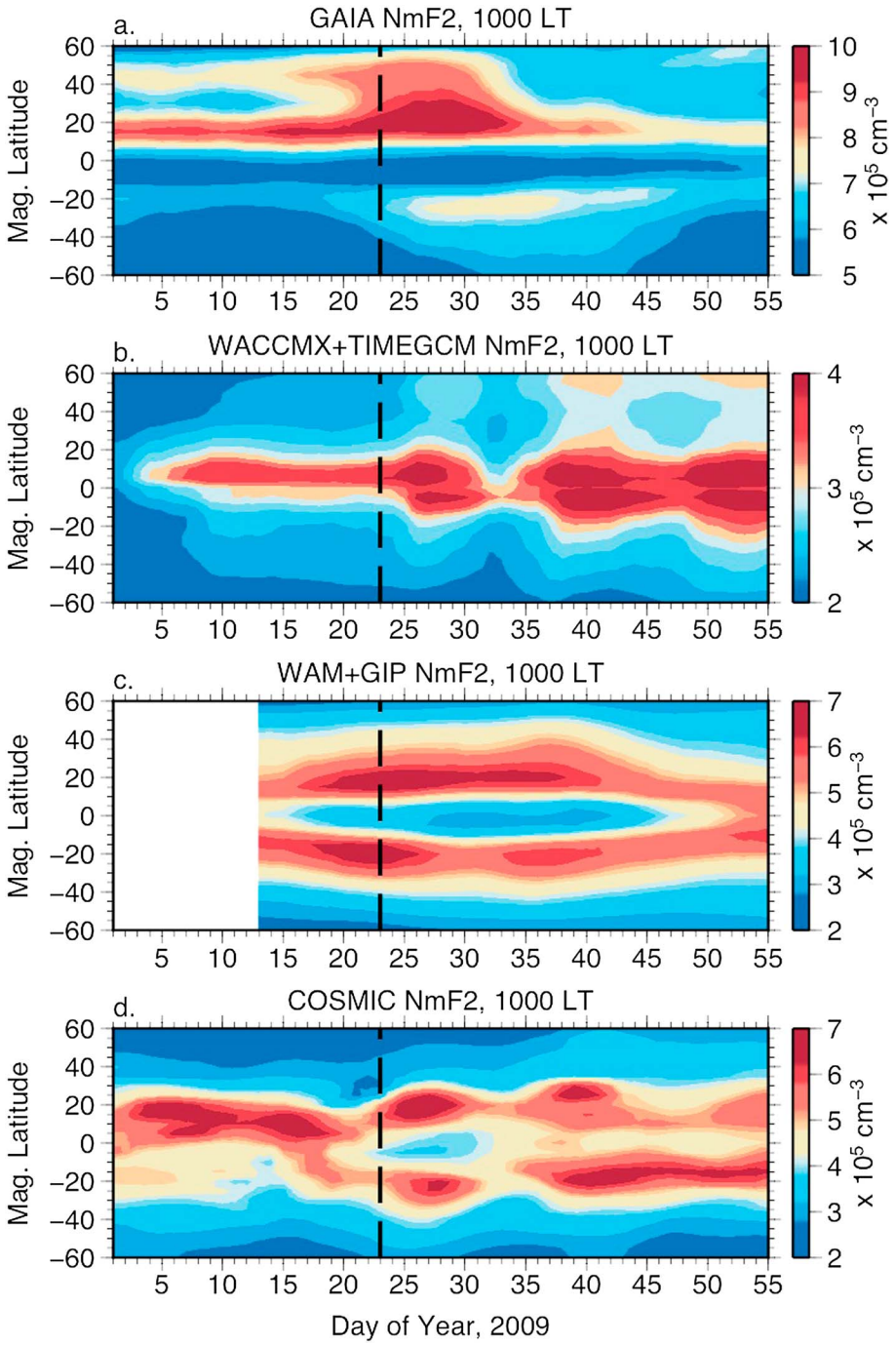

Figure 3. Zonal mean N_mF_2 at 1000 local time simulated by the (a) GAIA, (b) WACCMX+TIMEGCM, and (c) WAM+GIP models, and (d) observed by COSMIC. Results are based on a 5 day running mean. The dashed vertical black line indicates the timing of the polar vortex weakening.

anomalies is too narrow. The narrow latitudinal width of the equatorial anomalies in WACCMX+TIMEGCM is thought to be related to possible deficiencies in the TIMEGCM during low solar flux conditions, and we note that the equatorial anomaly width is more consistent with observations during solar moderate and maximum conditions. This could also be related to the model upper boundary, and the specified upper boundary flux, but the impact of the low model upper boundary is thought to be small during solar minimum, geomagnetic quiet, conditions. It should also be considered that the WACCMX+TIMEGCM equatorial anomalies tend to be wider in the early afternoon, when the crests are near ±10–15° (not shown). The narrow width of the

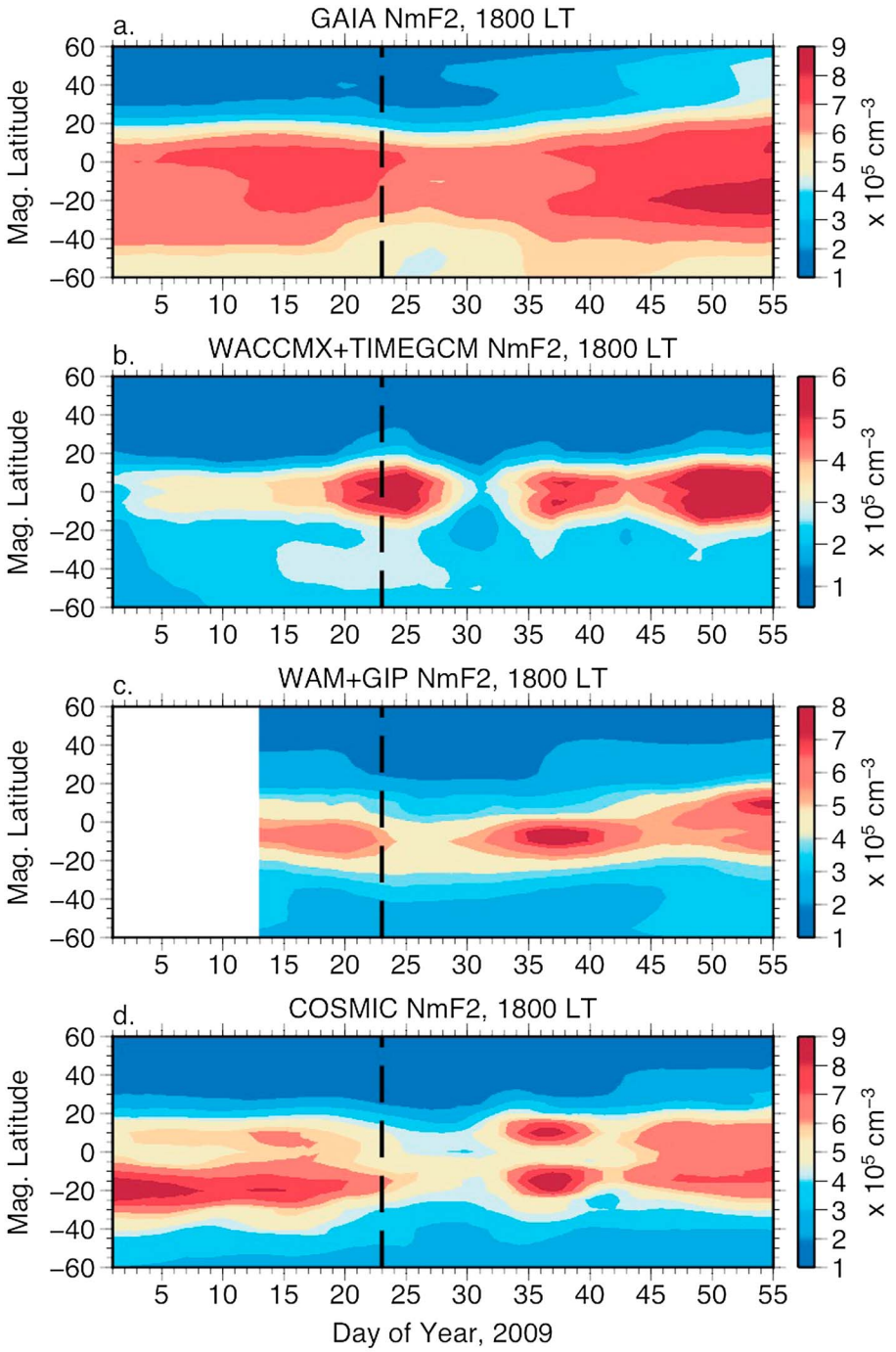

Figure 4. Zonal mean N_mF_2 at 1800 local time simulated by the (a) GAIA, (b) WACCMX+TIMEGCM, and (c) WAM+GIP models, and (d) observed by COSMIC. Results are based on a 5 day running mean. The dashed vertical black line indicates the timing of the polar vortex weakening.

equatorial anomalies is thus partially related to the local times that are shown in Figures 3 and 4. The three different model simulations capture the temporal variability that is seen in the observations with varying degrees of success. The agreement is best at 1800 LT, when all of the model simulations are able to capture the observed N_mF_2 decrease following the SSW, though the timing of this decrease differs among the simulations. The consistency of the model simulations, and agreement with the observations, is worse at 1000 LT. At this local time, only the WACCMX+TIMEGCM simulation is able to capture the short-term variability seen in the observations. The N_mF_2 minimum that occurs around days 30–35 at 1000 LT is absent in the GAIA simulation

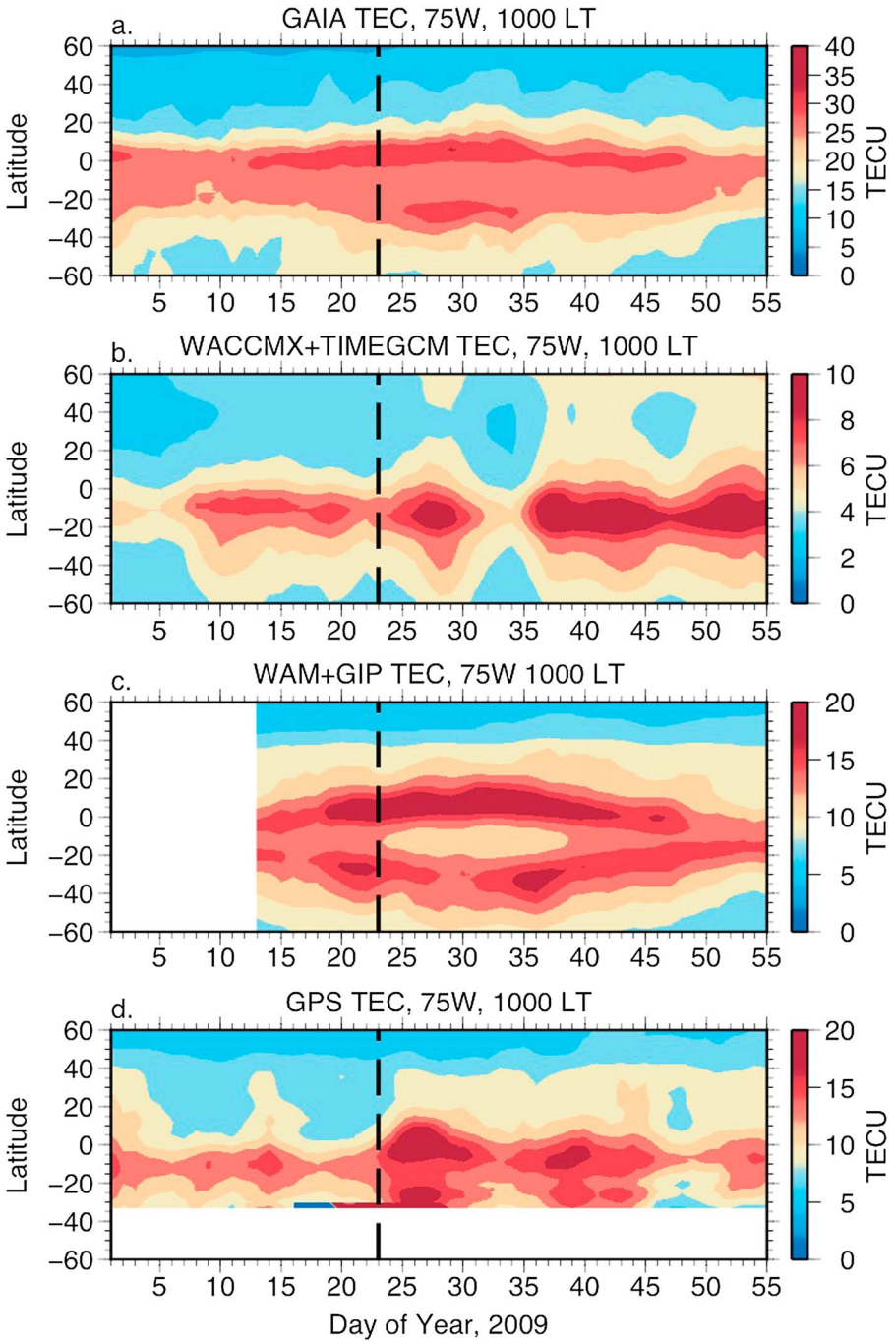

Figure 5. Total electron content at 1000 local time simulated by the (a) GAIA, (b) WACCMX+TIMEGCM, and (c) WAM+GIP models, and (d) observed by ground-based GPS receivers. The dashed vertical black line indicates the timing of the polar vortex weakening.

and only apparent in WAM+GIP in the Southern Hemisphere. The inability of the GAIA and WAM+GIP simulations to adequately reproduce the variability in the morning may be related to the extended periods of enhanced morning upward vertical drift perturbations (Figures 1 and 2) that are seen in these simulations.

Comparisons of the model simulations of TEC with the ground-based GPS observations at 75°W at 1000 and 1800 LT are presented in Figures 5 and 6, respectively. Note that the TEC observations poleward of 35°S are not shown due to poor data quality resulting from the sparse observation coverage at these latitudes. Similar to the vertical plasma drift perturbations, a 3 day smoothing has been applied to the simulated and

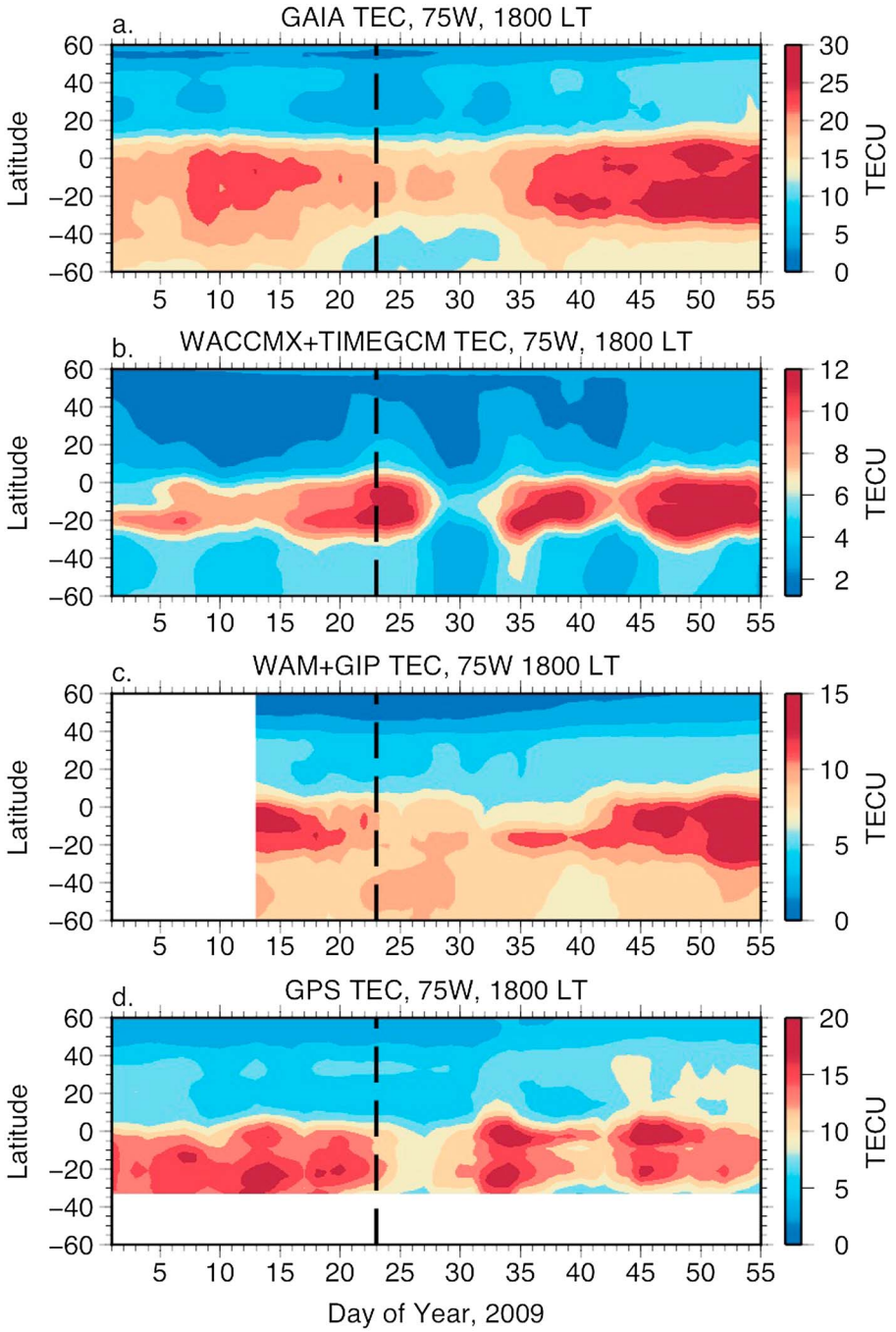

Figure 6. Total electron content at 1800 local time simulated by the (a) GAIA, (b) WACCMX+TIMEGCM, and (c) WAM+GIP models, and (d) observed by ground-based GPS receivers. The dashed vertical black line indicates the timing of the polar vortex weakening.

observed TEC. We reiterate that the TEC comparison should be considered in a qualitative sense since the model upper boundaries inhibit a direct, quantitative, comparison. The TEC at 75°W displays largely similar features to the zonal mean N_mF_2. The similarities and differences between the different model simulations and the GPS TEC observations are also similar to the comparison of N_mF_2. In particular, it is again evident that the GAIA and WAM+GIP simulations show extended periods of enhanced TEC at 1000 LT. This is in contrast to the WACCMX+TIMEGCM simulation and ground-based GPS TEC observations which indicate that the enhancement occurring after the SSW onset only occurs between days 25 and 30, and is followed by a short-term decrease in TEC between days 30 and 5. These differences are again attributed to the extended

period of enhanced vertical plasma drifts in the morning in the GAIA and WAM+GIP simulations (Figure 1). Discrepancies between the observed and modeled TEC are therefore in large part due the inability of the model simulations to capture the observed vertical plasma drift perturbations. An additional source of the discrepancies may be due to differences in the simulated thermosphere neutral composition which may result from the impact of tidal dissipation on the thermosphere circulation [*Yamazaki and Richmond*, 2013; *Shpynev et al.*, 2015]. We do, however, consider effects due to the thermosphere composition to be of secondary importance compared to electrodynamics, at least at low latitudes. The three model simulations are significantly better at reproducing the observations at 1800 LT, and all of the models capture the decrease following the SSW onset. However, the timing and extent of this decrease differ among the model simulations, and between the simulations and observations. For example, the GAIA and WAM+GIP models do not capture the short-term increase in TEC that occurs just prior to day 35. This feature is seen in the WACCMX+TIMEGCM simulations, although it is delayed by a few days compared to the observations.

Based on the comparisons in Figures 1–4 it is clear that, although the models may be able to capture general features of ionosphere variability during the SSW, there are significant differences among the individual model simulations. Furthermore, there remain clear discrepancies between the simulations and observations, with none of the model simulations able to capture all aspects of the variability that is seen in the observations.

4.2. Sensitivity to Neutral Atmosphere Forcing

We now turn our attention to understanding the impact of differences in the neutral atmosphere on the simulated ionosphere variability during the 2009 SSW. The reader is referred to *Pedatella et al.* [2014b] for a comprehensive discussion regarding the differences in the neutral atmosphere simulations. The aspect of the prior comparison that is thought to be most relevant to the present study are the amplitude and temporal variability of the *SW*2. In brief, *Pedatella et al.* [2014b] found that although all of the simulations exhibit similar temporal variability, the amplitude of the *SW*2 differs significantly among the simulations. The WACCMX *SW*2 amplitude is approximately 20% of the WAM amplitude, and the GAIA and HAMMONIA simulations fall roughly in the middle of the WACCMX and WAM values. These differences are considered especially relevant since the *SW*2 has a significant impact on the equatorial electrodynamics [e.g., *Fesen et al.*, 2000]. The change in the *SW*2 phase during the SSW, which will impact the local time variability of the equatorial ionosphere perturbations, is similar among the four model simulations. Though not shown here, the nudging strongly constrains the different TIMEGCM simulations to their respective original simulations, at least up to the lower thermosphere. The different TIMEGCM simulations thus reflect the different tidal variabilities shown in *Pedatella et al.* [2014b].

The vertical drift perturbations in the American and Indian longitude sectors for the different TIMEGCM simulations along with the Jicamarca ISR and magnetometer ΔH observations are shown in Figures 7 and 8. We remind the reader that the WACCMX+TIMEGCM$_{ff}$ simulations shown here, and throughout the remainder of this section, differ from those presented in section 4.1 in that they do not include the *M*2 lunar tide and are nudged using the full dynamical fields up to ~95 km (as opposed to just the zonal mean). Nudging with the full dynamical fields results in a significantly weaker *SW*2 in the WACCMX+TIMEGCM$_{ff}$ simulation compared to the WACCMX+TIMEGCM simulation presented previously. The results in Figures 7 and 8 reveal that the simulated vertical plasma drift perturbations are generally similar when different neutral atmospheres are used as lower atmospheric forcing for the same ionosphere-thermosphere model. The similarity is clearly evident in terms of the progression of the drift perturbations toward later local times, which is seen to be very consistent among the simulations. This is not too surprising given the consistency in the *SW*2 phase changes among the model simulations, which is likely to be the source of the shift toward later local times. We note that the shift of the perturbations toward later local times is slower in all of the simulations than in the observations. Since none of the TIMEGCM simulations include the *M*2 lunar tide, the slow phase shift supports our prior assertion that the *M*2 lunar tide is important for fully capturing this feature. Although the simulations are largely similar, the impact of the different neutral atmospheres is also evident. It is clear that the magnitude of the drift perturbations generally follows the *SW*2 amplitude, with the WAM+TIMEGCM simulated drift perturbations being significantly larger than the other three models. The drift perturbations in the WACCMX+TIMEGCM$_{ff}$ simulations, which has by far the weakest *SW*2, are also small and it is difficult to discern a clear signature of the SSW in this simulation. These results clearly illustrate the importance of accurately modeling the tides at MLT altitudes for simulating the ionosphere variability.

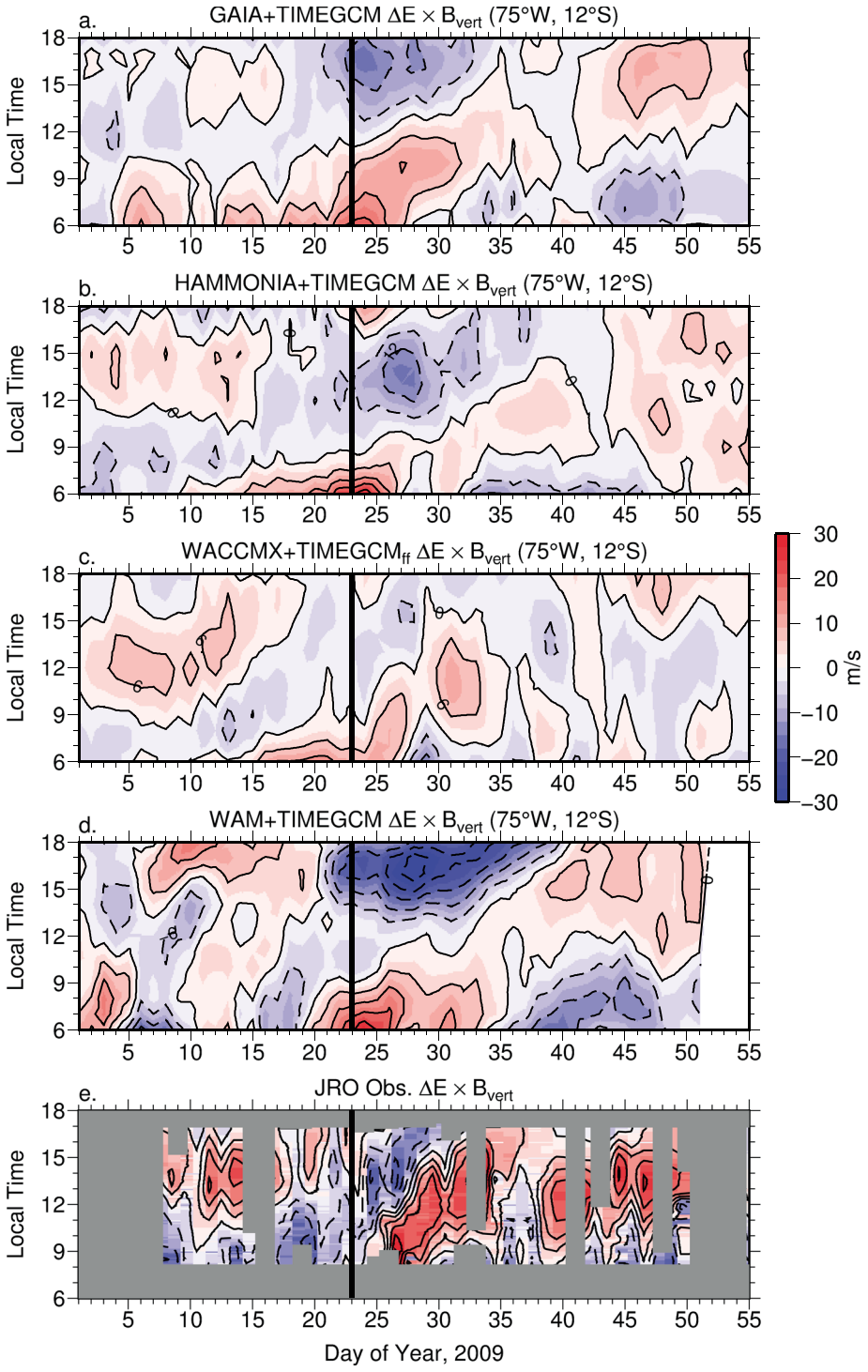

Figure 7. Perturbations in the vertical plasma drift at Jicamarca, Peru (75°W, 12°S) in the TIMEGCM simulations with lower atmosphere forcing from (a) GAIA, (b), HAMMONIA, (c), WACCMX, and (d) WAM. (e) The observed vertical plasma drift perturbations from the Jicamarca incoherent scatter radar. The gray areas in Figure 7e indicate periods when observations are unavailable. The solid vertical black line indicates the timing of the polar vortex weakening. Contours are every 6 m s^{-1}.

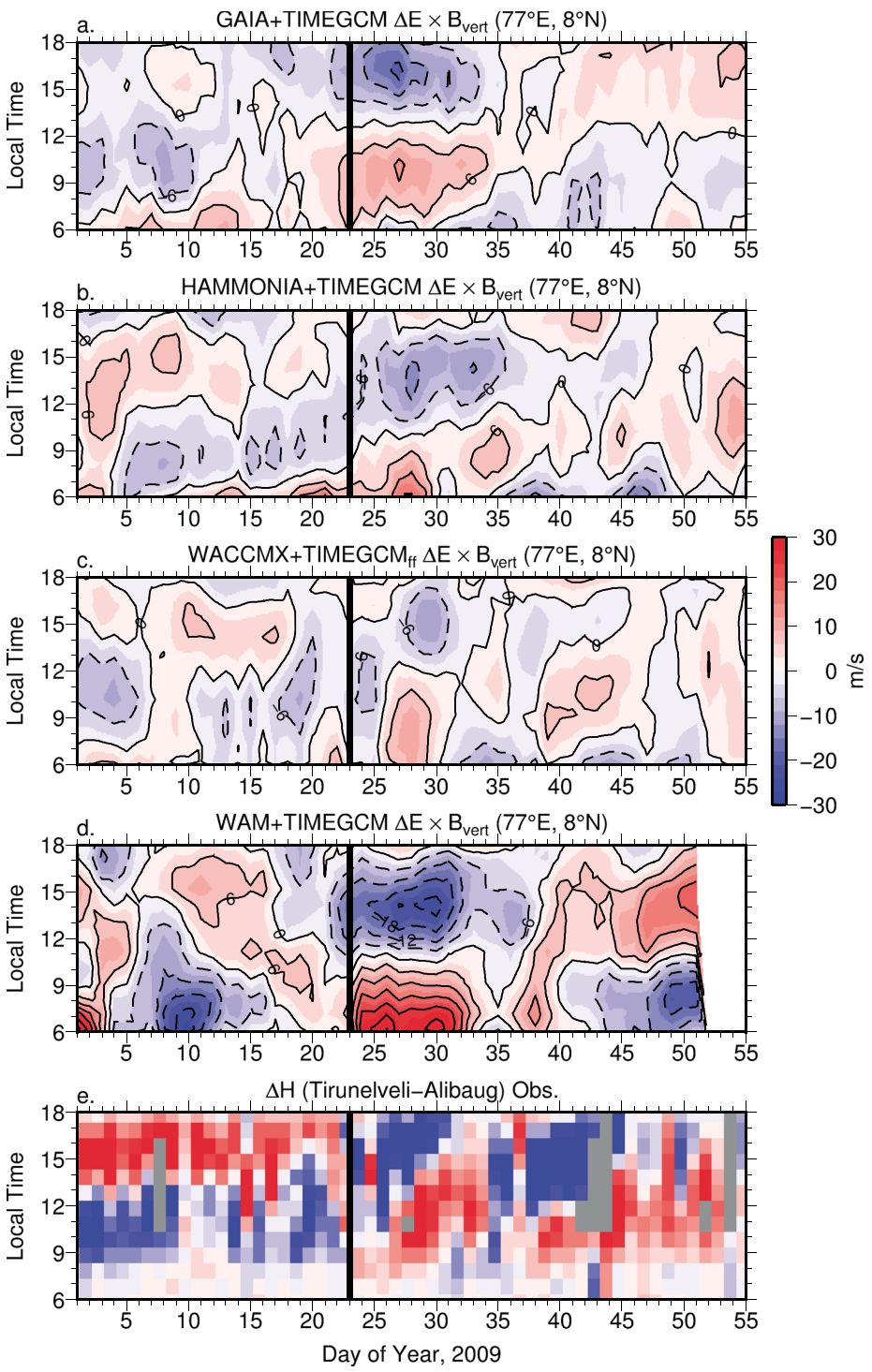

Figure 8. Perturbations in the vertical plasma drift velocity at Tirunelveli, India (77°E, 8°N) in the TIMEGCM simulations with lower atmosphere forcing from (a) GAIA, (b) HAMMONIA, (c) WACCMX, and (d) WAM. (e) Observed equatorial electrojet perturbations (ΔH) from differencing magnetometer observations at Tirunelveli and Alibaug. The gray areas in Figure 8e indicate periods when observations are unavailable. The solid vertical black line indicates the timing of the polar vortex weakening. Contours are every 6 m s^{-1}.

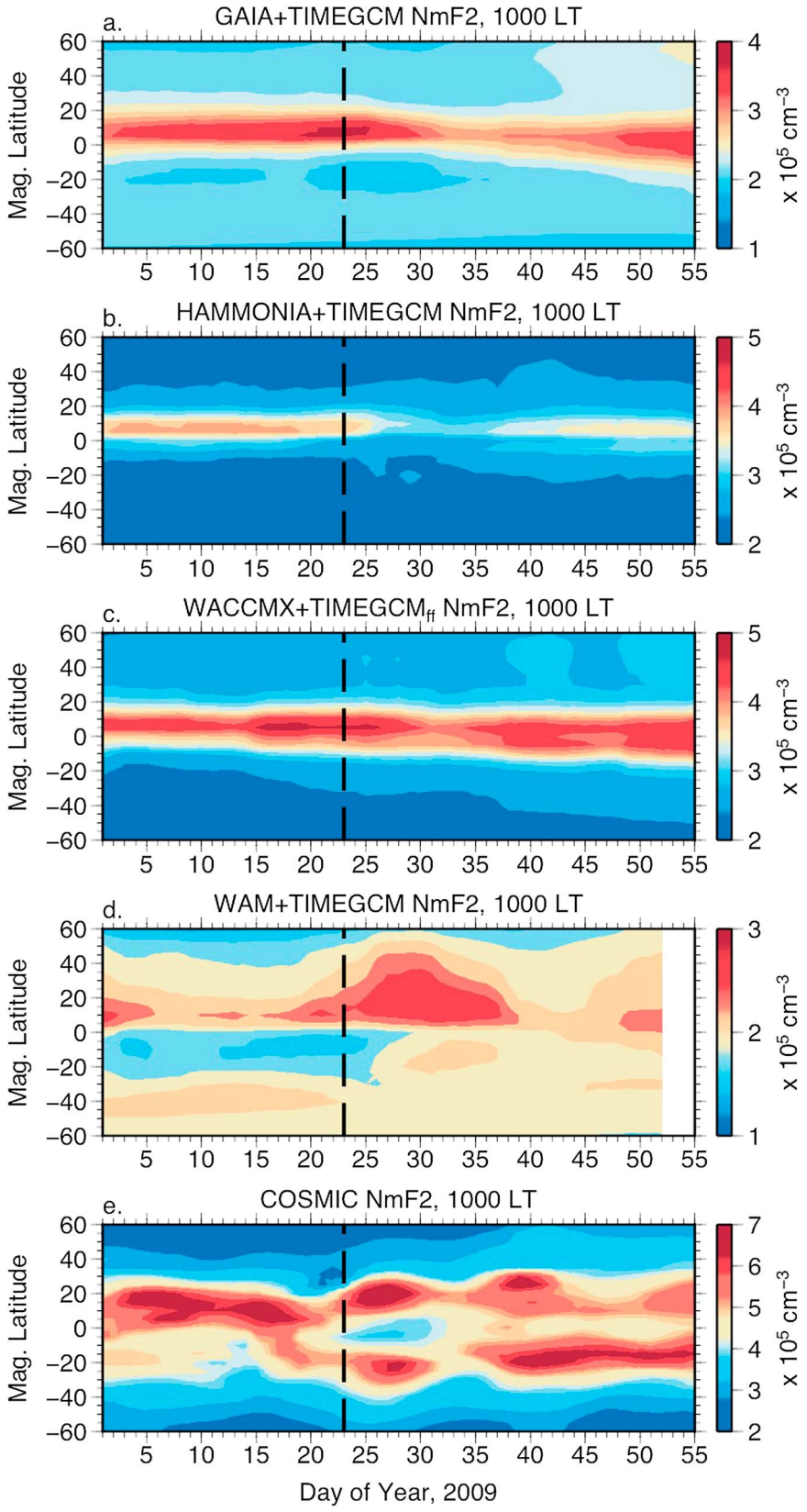

Figure 9. Zonal mean N_mF_2 at 1000 local time simulated by the TIMEGCM with lower atmosphere forcing from (a) GAIA, (b) HAMMONIA, (c) WACCMX, and (d) WAM, and (e) observed by COSMIC. Results are based on a 5 day running mean. The dashed vertical black line indicates the timing of the polar vortex weakening.

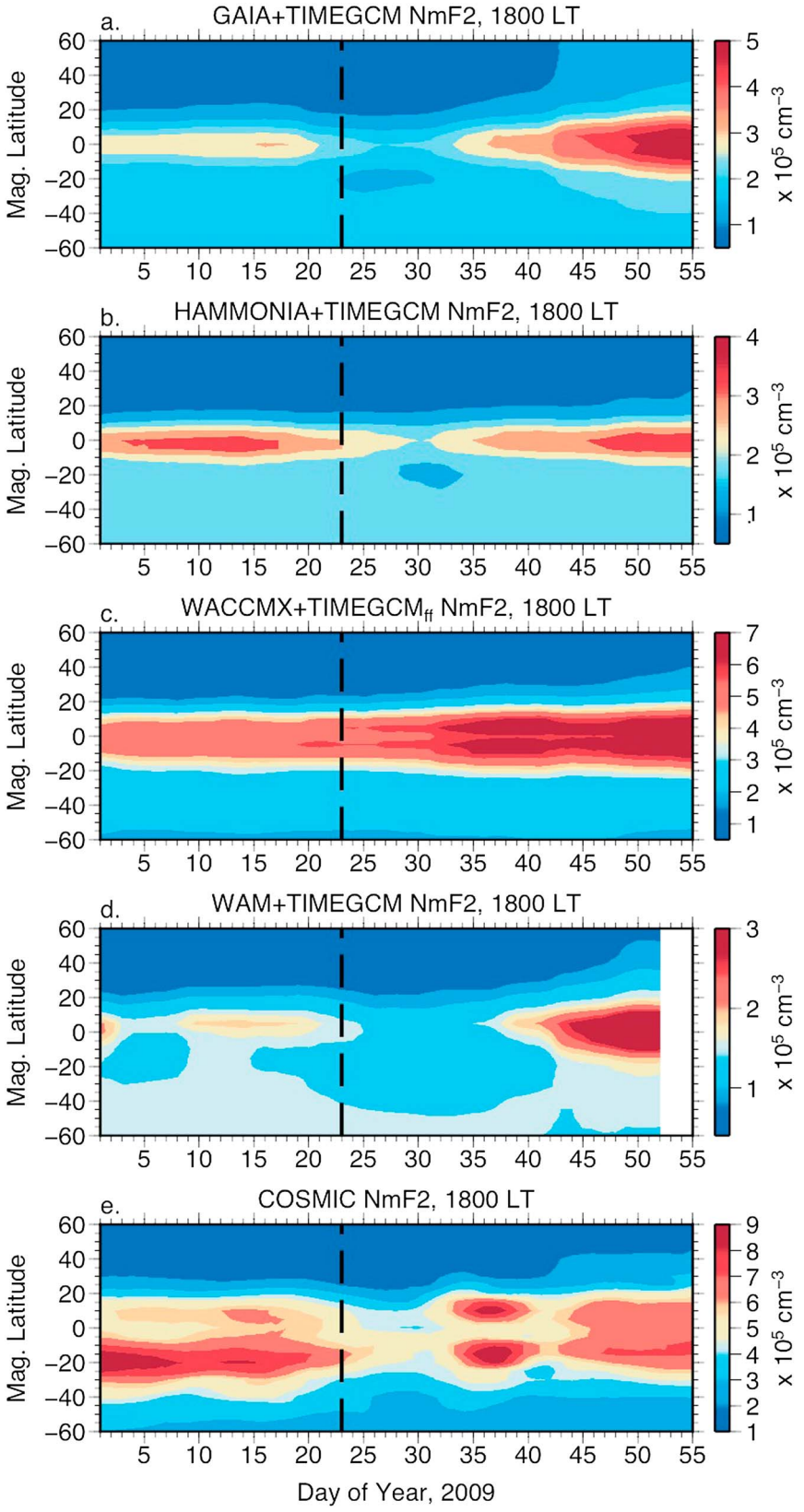

Figure 10. Zonal mean N_mF_2 at 1800 local time simulated by the TIMEGCM with lower atmosphere forcing from (a) GAIA, (b) HAMMONIA, (c) WACCMX, and (d) WAM, and (e) observed by COSMIC. Results are based on a 5 day running mean. The dashed vertical black line indicates the timing of the polar vortex weakening.

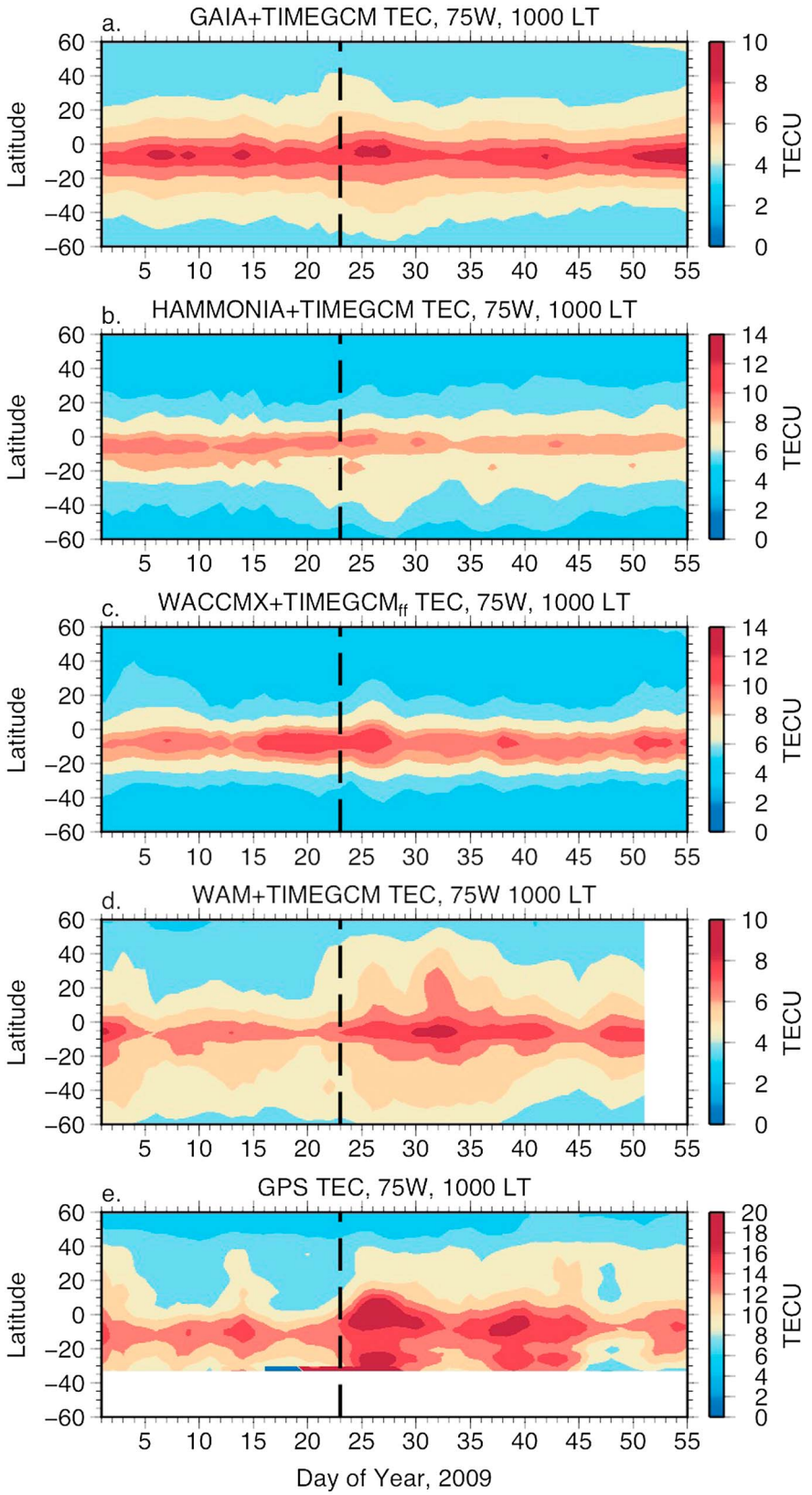

Figure 11. Total electron content at 1000 local time simulated by the TIMEGCM with lower atmosphere forcing from (a) GAIA, (b) HAMMONIA, (c) WACCMX, and (d) WAM models, and (e) observed by ground-based GPS receivers. The dashed vertical black line indicates the timing of the polar vortex weakening.

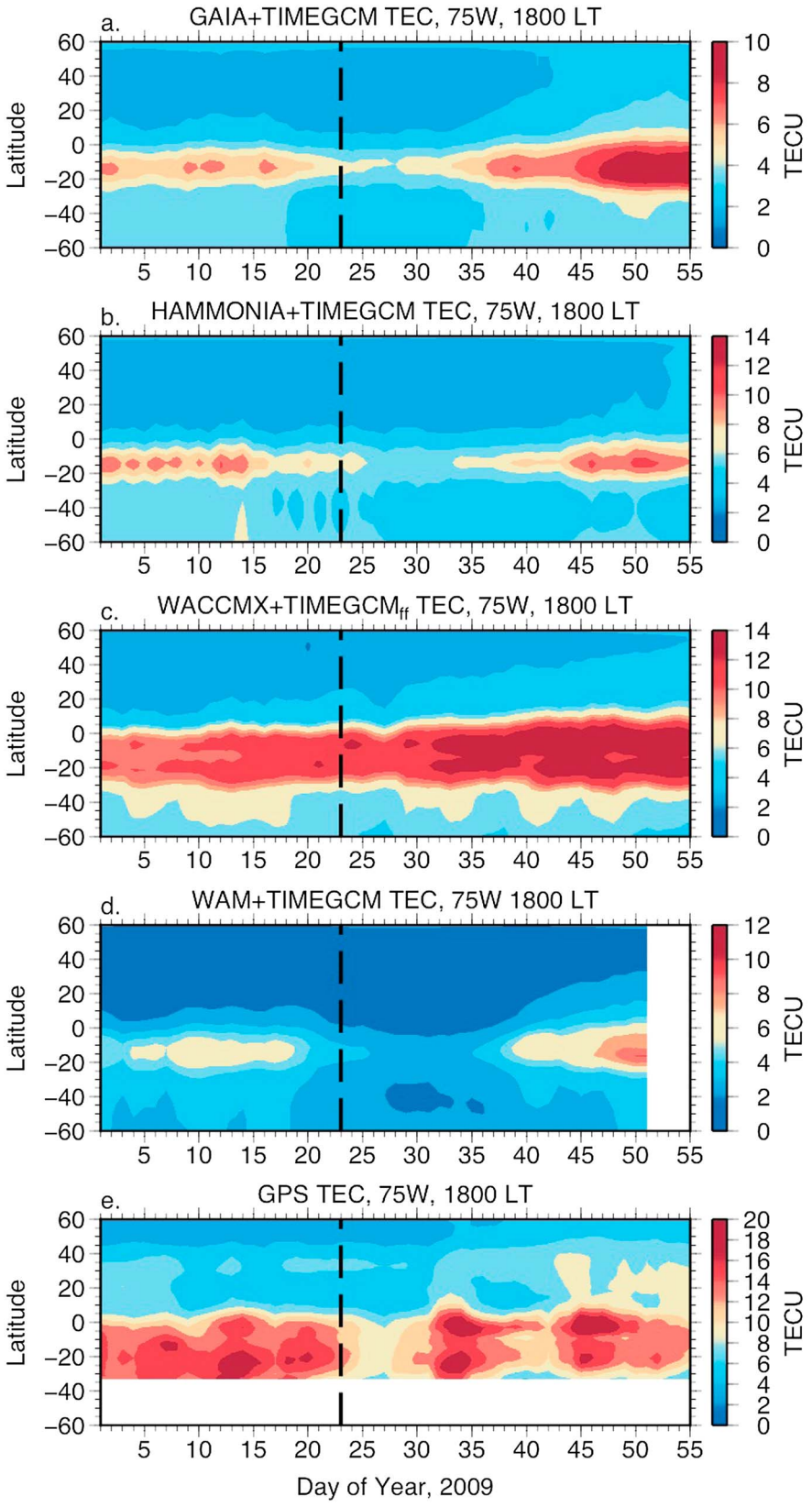

Figure 12. Total electron content at 1800 local time simulated by the TIMEGCM with lower atmosphere forcing from (a) GAIA, (b) HAMMONIA, (c) WACCMX, and (d) WAM models, and (e) observed by ground-based GPS receivers. The dashed vertical black line indicates the timing of the polar vortex weakening.

Figures 9–12 show the N_mF_2 and TEC at 1000 LT and 1800 LT simulated by the four different TIMEGCM simulations and N_mF_2 observed by COSMIC and the ground-based GPS TEC. There are clear differences among the model simulations, and this again demonstrates that differences in the simulated neutral atmosphere will impact the electron density. Weak to nonexistent equatorial anomalies are evident in Figures 9 and 10, indicating that this is apparently a general problem with the TIMEGCM. We reiterate that this is thought to be related to possible deficiencies in the TIMEGCM during extremely low solar flux conditions and also that the width of the anomalies is wider during the early afternoon. At 1000 LT, although the four TIMEGCM simulations capture some aspects of the observed variability, the notable disagreements with the observations illustrate that the simulations poorly capture the ionosphere electron density variability in the morning. The agreement at 1800 LT is generally better, and the GAIA, HAMMONIA, and WAM simulations all capture the decrease after the SSW; however, they fail to capture the observed short-term increase that occurs around day 35. We note that the WACCMX+TIMEGCM$_{ff}$ simulation fails to capture the decrease following the SSW at 1800 LT. The absence of this feature in the WACCMX+TIMEGCM$_{ff}$ simulation is attributed to the weak afternoon equatorial vertical drift perturbations (Figures 7 and 8). We again emphasize that the weak drifts are thought to be the result of the low *SW*2 amplitudes in WACCM-X. It should be mentioned that the *SW*2 in the model simulations that reproduce the magnitude of the observed vertical drift perturbations may be too large. If the *M*2 were added to these simulations, the local time behavior of the vertical drift perturbations may improve, but the magnitudes may also increase, resulting in vertical drift perturbations that are too great. These points illustrate the importance of accurately simulating the variability in the MLT in order to reliably reproduce the upper atmosphere variability during SSWs. Although the above discussion is focused on the N_mF_2, the TEC results at 1000 and 1800 LT (Figures 11 and 12) reveal similar features as the N_mF_2.

5. Summary and Conclusions

The present study extends *Pedatella et al.* [2014b] previous comparison of neutral atmosphere simulations of the 2009 SSW to the ionosphere. The primary focus is on the daytime equatorial and low-latitude ionosphere variability during the 2009 SSW simulated in GAIA, WAM+GIP, and WACCMX+TIMEGCM. Based on comparison with observations, we reach the following conclusions:

1. The model simulations are all capable of reproducing the observed morning enhancement and afternoon decrease of the equatorial vertical plasma drift that occurs ~2–3 days following the SSW onset in both the American and Indian longitude sectors. However, the magnitude of the variability differs among the simulations, which is thought to be related to differences in the simulated *SW*2 amplitudes.
2. The shift of the vertical drift perturbations toward later local times in the GAIA and WAM+GIP simulations occurs ~5 days later than seen in the observations. The WACCMX+TIMEGCM simulation well reproduces the local time shift. WACCMX+TIMEGCM is the only simulation that includes the *M*2 lunar tide, indicating the possible importance of the lunar tide for modulating the equatorial electrodynamics during the 2009 SSW.
3. All three model simulations can reproduce certain aspects of the observed zonal mean N_mF_2 variability and the ground-based GPS TEC at 75°W. There are, however, several features in the observations that are poorly reproduced, or absent, in the model simulations. The simulated variability overall tends to be in better agreement with the observations at 1800 LT compared to 1000 LT.

To assess the impact of differences in the neutral atmosphere on the simulated ionosphere variability, additional experiments were performed where the neutral atmospheres from GAIA, HAMMONIA, WACCM-X, and WAM were used to constrain the TIMEGCM up to ~95 km. The results of these simulations illustrate that the differences seen in comparing the GAIA, WAM+GIP, and WACCMX+TIMEGCM can be attributed to both differences in how the models simulate the ionospheric processes as well as differences in their neutral atmospheres. The amplitude and variability of the *SW*2 is thought to be especially important with regard to being able to reliably simulate the ionosphere variability during SSWs. This illustrates that accurately modeling variability in the MLT is essential for understanding the impact of SSWs on the ionosphere.

The present study is intended to provide an overview of the current capability to simulate the equatorial and low-latitude ionosphere variability during SSWs. Though the results are considered as generally representative of current modeling capabilities, it should be recognized that we have focused on a single, extremely strong, SSW event. Overall, the comparison demonstrates that although current models can reproduce general features of the SSW variability, they are all rather different, and each captures certain aspects of the variability better than the others. It is therefore necessary to continue to advance modeling capabilities both

through improvements in the underlying models themselves, as well as through possible improvements in methodology for constraining the simulations at ionospheric altitudes, for example, by implementing ionosphere-thermosphere data assimilation techniques. As the models continue to evolve, we anticipate the overall capability of reproducing the upper atmosphere variability during meteorological events to be improved in the future.

Acknowledgments
COSMIC electron density profile observations are distributed by the COSMIC Data Analysis and Archive Center (http://cdaac-www.cosmic.ucar.edu/cdaac/). The Jicamarca ISR and ground-based GPS TEC data are available through the MIT Haystack Observatory Madrigal database (http://madrigal.haystack.mit.edu/madrigal/). Simulation output is archived and available upon request. The magnetometer data are provided by the World Data Center for Geomagnetism (http://www.wdc.bgs.ac.uk/catalog/master.html). We acknowledge the International Space Science Institute for supporting an international team which led to the present model comparison. N.P. acknowledges support from National Science Foundation grant AGS-1522830. L.P.G. was supported by NASA through LWS grant NNX13AI62G and by the NSF through grant AGS-1132267. T.-W.F. acknowledges support from the NSF CEDAR Program award 1243129. F.S. was supported by the Chief of Naval Research.

References

Akmaev, R. A., T. J. Fuller-Rowell, F. Wu, J. M. Forbes, X. Zhang, A. F. Anghel, M. D. Iredell, S. Moorthi, and H. Juang (2008), Tidal variability in the lower thermosphere: Comparison of Whole Atmosphere Model (WAM) simulations with observations from TIMED, *Geophys. Res. Lett.*, *35*, L03810, doi:10.1029/2007GL032584.

Anderson, D., A. Anghel, K. Yumoto, M. Ishitsuka, and E. Kudeki (2002), Estimating daytime vertical $E \times B$ drift velocities in the equatorial F-region using ground-based magnetometer observations, *Geophys. Res. Lett.*, *29*(12), 1596, doi:10.1029/2001GL014562.

Anthes, R., et al. (2008), The COSMIC/FORMOSAT-3 mission: Early results, *Bull. Am. Meteorol. Soc.*, *89*, 313–333.

Chau, J. L., and R. F. Woodman (2004), Daytime vertical and zonal velocities from 150-km echoes: Their relevance to F-region dynamics, *Geophys. Res. Lett.*, *31*, L17801, doi:10.1029/2004GL020800.

Chau, J. L., B. G. Fejer, and L. P. Goncharenko (2009), Quiet variability of equatorial $E \times B$ drifts during a sudden stratospheric warming event, *Geophys. Res. Lett.*, *36*, L05101, doi:10.1029/2008GL036785.

Chau, J. L., L. P. Goncharenko, B. G. Fejer, and H.-L. Liu (2011), Equatorial and low latitude ionospheric effects during sudden stratospheric warming events, *Space Sci. Rev.*, *168*, 385–417, doi:10.1007/s11214-011-9797-5.

Fagundes, P. R., L. P. Goncharenko, A. J. de Abreu, K. Venkatesh, M. Pezzopane, R. de Jesus, M. Gende, A. J. Coster, and V. G. Pillat (2015), Ionospheric response to the 2009 sudden stratospheric warming over the equatorial, low, and middle latitudes in the South American sector, *J. Geophys. Res.*, *120*(9), 7889–7902, doi:10.1002/2014JA020649.

Fang, T., H. Kil, G. Millward, A. D. Richmond, J. Liu, and S. Oh (2009), Causal link of the wave-4 structures in plasma density and vertical plasma drift in the low-latitude ionosphere, *J. Geophys. Res.*, *114*, A10315, doi:10.1029/2009JA014460.

Fang, T.-W., T. Fuller-Rowell, R. Akmaev, F. Wu, H. Wang, and D. Anderson (2012), Longitudinal variation of ionospheric vertical drifts during the 2009 sudden stratospheric warming, *J. Geophys. Res.*, *117*, A03324, doi:10.1029/2011JA017348.

Fang, T.-W., T. Fuller-Rowell, H. Wang, R. Akmaev, and F. Wu (2014a), Ionospheric response to sudden stratospheric warming events at low and high solar activity, *J. Geophys. Res.*, *119*, 7858–7869, doi:10.1002/2014JA020142.

Fang, T.-W., et al. (2014b), Comparative studies of theoretical models in the equatorial ionosphere, in *Modeling the Ionosphere-Thermosphere System*, edited by J. Huba, R. Schunk, and G. Khazanov, pp. 133–144, John Wiley, Chichester, U. K.

Fejer, B. G., M. E. Olson, J. L. Chau, C. Stolle, H. Lühr, L. P. Goncharenko, K. Yumoto, and T. Nagatsuma (2010), Lunar-dependent equatorial ionospheric electrodynamic effects during sudden stratospheric warmings, *J. Geophys. Res.*, *115*, A00G03, doi:10.1029/2010JA015273.

Fesen, C. G., G. Crowley, R. G. Roble, A. D. Richmond, and B. G. Fejer (2000), Simulation of the pre-reversal enhancement in the low latitude vertical ion drifts, *Geophys. Res. Lett.*, *27*(13), 1851–1854, doi:10.1029/2000GL000061.

Forbes, J. M., and X. Zhang (2012), Lunar tide amplification during the January 2009 stratosphere warming event: Observations and theory, *J. Geophys. Res.*, *117*, A12312, doi:10.1029/2012JA017963.

Fuller-Rowell, T., F. Wu, R. Akmaev, T.-W. Fang, and E. Araujo-Pradere (2010), A whole atmosphere model simulation of the impact of a sudden stratospheric warming on thermosphere dynamics and electrodynamics, *J. Geophys. Res.*, *115*, A00G08, doi:10.1029/2010JA015524.

Funke, B., M. López-Puertas, D. Bermejo-Pantaleón, M. García-Comas, G. P. Stiller, T. von Clarmann, M. Kiefer, and A. Linden (2010), Evidence for dynamical coupling from the lower atmosphere to the thermosphere during a major stratospheric warming, *Geophys. Res. Lett.*, *37*, L13803, doi:10.1029/2010GL043619.

Goncharenko, L. P., A. J. Coster, J. L. Chau, and C. E. Valladares (2010a), Impact of sudden stratospheric warmings on equatorial ionization anomaly, *J. Geophys. Res.*, *115*, A00G07, doi:10.1029/2010JA015400.

Goncharenko, L. P., J. L. Chau, H.-L. Liu, and A. J. Coster (2010b), Unexpected connections between the stratosphere and ionosphere, *Geophys. Res. Lett.*, *37*, L10101, doi:10.1029/2010GL043125.

Goncharenko, L., J. L. Chau, P. Condor, A. Coster, and L. Benkevitch (2013), Ionospheric effects of sudden stratospheric warming during moderate-to-high solar activity: Case study of January 2013, *Geophys. Res. Lett.*, *40*, 4982–4986, doi:10.1002/grl.50980.

Jin, H., Y. Miyoshi, D. Pancheva, P. Mukhtarov, H. Fujiwara, and H. Shinagawa (2012), Response of migrating tides to the stratospheric sudden warming in 2009 and their effects on the ionosphere studied by a whole atmosphere-ionosphere model GAIA with COSMIC and TIMED/SABER observations, *J. Geophys. Res.*, *117*, A10323, doi:10.1029/2012JA017650.

Jonah, O. F., E. R. de Paula, E. A. Kherani, S. L. G. Dutra, and R. R. Paes (2014), Atmospheric and ionospheric response to sudden stratospheric warming of January 2013, *J. Geophys. Res. Space Physics*, *119*, 4973–4980, doi:10.1002/2013JA019491.

Klimenko, M. V., V. V. Klimenko, F. S. Bessarab, Y. N. Korenkov, H. Liu, L. P. Goncharenko, and M. V. Tolstikov (2015a), Study of the thermospheric and ionospheric response to the 2009 sudden stratospheric warming using TIME-GCM and GSM TIP models: First results, *J. Geophys. Res. Space Physics*, *120*, 7873–7888, doi:10.1002/2014JA020861.

Klimenko, M. V., V. V. Klimenko, I. E. Zakharenkova, and I. V. Cherniak (2015b), The global morphology of the plasmaspheric electron content during Northern winter 2009 based on GPS/COSMIC observation and GSM TIP model results, *Adv. Space Res.*, *55*, 2007–2085, doi:10.1016/j.asr.2014.06.027.

Klimenko, M. V., V. V. Klimenko, F. S. Bessarb, Y. N. Korenkov, E. V. Rozanov, T. Reddmann, I. E. Zakharenkova, and M. V. Tolstikov (2016), Application of the models of the middle and upper atmosphere to simulation of total electron content perturbations caused by the 2009 stratospheric warming, *Russ. J. Phys. Chem. B*, *10*(1), 109–116.

Korenkov, Y. N., et al. (2012), The global thermospheric and ionospheric response to the 2008 minor sudden stratospheric warming event, *J. Geophys. Res.*, *117*, A10309, doi:10.1029/2012JA018018.

Lee, H.-B., G. Jee, Y. H. Kim, and J. S. Shim (2013), Characteristics of global plasmaspheric TEC in comparison with the ionosphere simultaneously observed by Jason-1 satellite, *J. Geophys. Res. Space Physics*, *118*, 935–946, doi:10.1002/jgra.50130.

Lei, J., et al. (2007), Comparison of COSMIC ionospheric measurements with ground-based observations and model predictions: Preliminary results, *J. Geophys. Res.*, *112*, A07308, doi:10.1029/2006JA012240.

Lin, C. H., J. T. Lin, L. C. Chang, J. Y. Liu, C. H. Chen, W. H. Chen, H. H. Huang, and C. H. Liu (2012), Observations of global ionospheric responses to the 2009 stratospheric sudden warming event by FORMOSAT-3/COSMIC, *J. Geophys. Res.*, *117*, A06323, doi:10.1029/2011JA017230.

Lin, C. H., J. T. Lin, L. C. Chang, W. H. Chen, C. H. Chen, and J. Y. Liu (2013), Stratospheric sudden warming effects on the ionospheric migrating tides during 2008–2010 observed by FORMOSAT-3/COSMIC, *J. Atmos. Sol. Terr. Phys.*, *103*, 66–75.

Liu, H., E. Doornbos, M. Yamamoto, and S. Tulasi Ram (2011), Strong thermospheric cooling during the 2009 major stratosphere warming, *Geophys. Res. Lett.*, *38*, L12102, doi:10.1029/2011GL047898.

Liu, H.-L., and R. G. Roble (2002), A study of a self-generated stratospheric sudden warming and its mesospheric-lower thermospheric impacts using the coupled TIME-GCM/CCM3, *J. Geophys. Res.*, *107*(D23), 4695, doi:10.1029/2001JD001533.

Liu, H.-L., W. Wang, A. D. Richmond, and R. G. Roble (2010), Ionospheric variability due to planetary waves and tides for solar minimum conditions, *J. Geophys. Res.*, *115*, A00G01, doi:10.1029/2009JA015188.

Liu, H.-L., V. A. Yudin, and R. G. Roble (2013), Day-to-day ionospheric variability due to lower atmosphere perturbations, *Geophys. Res. Lett.*, *40*, 665–670, doi:10.1002/grl.50125.

Manney, G. L., M. J. Schwartz, K. Krüger, M. L. Santee, S. Pawson, J. N. Lee, W. H. Daffer, R. A. Fuller, and N. J. Livesey (2009), Aura Microwave Limb Sounder observations of dynamics and transport during the record-breaking 2009 Arctic stratospheric major warming, *Geophys. Res. Lett.*, *36*, L12815, doi:10.1029/2009GL038586.

Maute, A., M. E. Hagan, A. D. Richmond, and R. G. Roble (2014), TIME-GCM study of the ionospheric equatorial vertical drift changes during the 2006 stratospheric sudden warming, *J. Geophys. Res. Space Physics*, *119*, 1287–1305, doi:10.1002/2013JA019490.

McDonald, S. E., F. Sassi, and A. J. Mannucci (2015), SAMI3/SD-WACCM-X simulations of ionospheric variability during Northern winter 2009, *Space Weather*, *13*, 568–584, doi:10.1002/2015SW001223.

McNamara, L. F., and D. C. Thompson (2014), Validation of COSMIC values of f_oF_2 and $M(3000)F_2$ using ground-based ionosondes, *Adv. Space Res.*, *55*, 163–169.

Medvedeva, I., A. Medvedev, K. Ratovsky, A. Shcherbakov, and M. Tolstikov (2015), Comprehensive study of disturbances of the neutral atmosphere and ionosphere parameters over Eastern Siberia during the 2013 January major sudden stratospheric warming, *Adv. Space Res.*, *56*, 1877–1885.

Pancheva, D., and P. Mukhtarov (2011), Stratospheric warmings: The atmosphere-ionosphere coupling paradigm, *J. Atmos. Sol. Terr. Phys.*, *73*(13), 1697–1702, doi:10.1016/j.jastp.2011.03.006.

Park, J., H. Lühr, M. Kunze, B. G. Fejer, and K. W. Min (2012), Effect of sudden stratospheric warming on lunar tidal modulation of the equatorial electrojet, *J. Geophys. Res.*, *117*, A03306, doi:10.1029/2011JA017351.

Pedatella, N. M., and H.-L. Liu (2013), The influence of atmospheric tide and planetary wave variability during sudden stratosphere warmings on the low latitude ionosphere, *J. Geophys. Res. Space Physics*, *118*, 5333–5347, doi:10.1002/jgra.50492.

Pedatella, N. M., and A. Maute (2015), Impact of the semidiurnal lunar tide on the midlatitude thermospheric wind and ionosphere during sudden stratosphere warmings, *J. Geophys. Res. Space Physics*, *120*, 10,740–10,753, doi:10.1002/2015JA021986.

Pedatella, N. M., H.-L. Liu, A. D. Richmond, A. Maute, and T.-W. Fang (2012), Simulations of solar and lunar tidal variability in the mesosphere and lower thermosphere during sudden stratosphere warmings and their influence on the low-latitude ionosphere, *J. Geophys. Res.*, *117*, A08326, doi:10.1029/2012JA017858.

Pedatella, N. M., H.-L. Liu, F. Sassi, J. Lei, J. L. Chau, and X. Zhang (2014a), Ionosphere variability during the 2009 SSW: Influence of the lunar semidiurnal tide and mechanisms producing electron density variability, *J. Geophys. Res. Space Physics*, *119*(5), 3828–3843, doi:10.1002/2014JA019849.

Pedatella, N. M., et al. (2014b), The neutral dynamics during the 2009 sudden stratosphere warming simulated by different whole atmosphere models, *J. Geophys. Res. Space Physics*, *119*, 1306–1324, doi:10.1002/2013JA019421.

Picone, J. M., A. E. Hedin, D. P. Drob, and A. C. Aikin (2002), NRLMSISE-00 empirical model of the atmosphere: Statistical comparisons and scientific issues, *J. Geophys. Res.*, *107*(A12), 1468, doi:10.1029/2002JA009430.

Polyakova, A. S., M. A. Chernigovkaya, and N. P. Perevalova (2014), Ionospheric effects of sudden stratospheric warmings in Eastern Siberia region, *J. Atmos. Sol. Terr. Phys.*, *120*, 15–23.

Richmond, A. D. (1995), Ionospheric electrodynamics using magnetic Apex coordinates, *J. Geomag. Geoelectr.*, *47*, 191–212.

Rideout, W., and A. Coster (2006), Automated GPS processing for global total electron content data, *GPS Solutions*, *10*(3), 219–228, doi:10.1007/s10291-006-0029-5.

Rodrigues, F. S., G. Crowley, S. M. I. Azeem, and R. A. Heelis (2011), C/NOFS observations of the equatorial ionospheric electric field response to the 2009 major sudden stratospheric warming event, *J. Geophys. Res.*, *116*, A09316, doi:10.1029/2011JA016660.

Sassi, F., H.-L. Liu, J. Ma, and R. R. Garcia (2013), The lower thermosphere during the Northern Hemisphere winter of 2009: A modeling study using high-altitude data assimilation products in WACCM-X, *J. Geophys. Res. Atmos.*, *118*, 8954–8968, doi:10.1002/jgrd.50632.

Sassi, F., H.-L. Liu, and J. T. Emmert (2016), Traveling planetary-scale waves in the lower thermosphere: Effects on neutral density and composition during solar minimum conditions, *J. Geophys. Res. Space Physics*, *121*, 1780–1801, doi:10.1002/2015JA022082.

Schmidt, H., G. P. Brasseur, M. Charron, E. Manzini, M. A. Giorgetta, T. Diehl, V. I. Formichev, D. Kinnison, D. Marsh, and S. Walters (2006), The HAMMONIA chemistry climate model: Sensitivity of the mesopause region to the 11-year solar cycle and CO_2 doubling, *J. Clim.*, *19*, 3903–3931, doi:10.1175/JCLI3829.1.

Shpynev, B. G., V. I. Kurkin, K. G. Ratovsky, M. A. Chernigovskaya, A. Y. Belinskaya, S. A. Grigorieva, A. E. Stepanov, V. V. Bychkov, D. Pancheva, and P. Mukhtarov (2015), High-midlatitude ionosphere response to major stratospheric warming, *Earth Planets Space*, *67*, doi:10.1186/s40623-015-0187-1.

Siddiqui, T. A., H. Lühr, C. Stolle, and J. Park (2015), Relation between stratospheric sudden warming and the lunar effect on the equatorial electrojet based on Huancayo recordings, *Ann. Geophys.*, *33*, 235–243, doi:10.5194/angeo-33-235-2015.

Shim, J. S., et al. (2011), CEDAR Electrodynamics Thermosphere Ionosphere (ETI) challenge for systematic assessment of ionosphere/thermosphere models: N_mF_2, H_mF_2, and vertical drift using ground-based observations, *Space Weather*, *9*, S12003, doi:10.1029/2011SW000727.

Wang, H., T. J. Fuller-Rowell, R. A. Akmaev, M. Hu, D. T. Kleist, and M. D. Iredell (2011), First simulations with a whole atmosphere data assimilation and forecast system: The January 2009 major sudden stratospheric warming, *J. Geophys. Res.*, *116*, A12321, doi:10.1029/2011JA017081.

Wang, H., R. A. Akmaev, T.-W. Fang, T. J. Fuller-Rowell, F. Wu, N. Maruyama, and M. D. Iredell (2014), First forecast of a sudden stratospheric warming with a coupled whole-atmosphere/ionosphere model IDEA, *J. Geophys. Res. Space Physics*, *119*, 2079–2089, doi:10.1002/2013JA019481.

Wu, Q., and S. Nozawa (2015), Mesospheric and thermospheric observations of the 2010 stratospheric warming event, *J. Atmos. Sol. Terr. Phys.*, *123*, 22–38.

Zhang, X., and J. M. Forbes (2014), Lunar tide in the thermosphere and weakening of the northern polar vortex, *Geophys. Res. Lett.*, *41*, 8201–8207, doi:10.1002/2014GL062103.

Yamazaki, Y., and A. D. Richmond (2013), A theory of ionospheric response to upward-propagating tides: Electrodynamic effects and tidal mixing effects, *J. Geophys. Res. Space Physics*, *118*, 5891–5905, doi:10.1002/jgra.50487.

Yiğit, E., and A. S. Medvedev (2015), Internal wave coupling processes in Earth's atmosphere, *Adv. Space Res.*, *55*, 983–1003.

Yizengaw, E., M. B. Moldwin, D. Galvan, B. A. Iijima, A. Komjathy, and A. J. Mannucci (2008), Global plasmaspheric TEC and its relative contribution to GPS TEC, *J. Atmos. Sol. Terr. Phys.*, *70*, 1541–1548.

Yue, X., W. S. Schreiner, N. Pedatella, R. A. Anthes, A. J. Mannucci, P. R. Straus, and J.-Y. Liu (2014), Space weather observations by GNSS radio occultation: From FORMOSAT-3/COSMIC to FORMOSAT-7/COSMIC-2, *Space Weather*, *12*, 616–621, doi:10.1002/2014SW001133.